Supplement of Atmos. Chem. Phys., 18, 11813–11829, 2018
https://doi.org/10.5194/acp-18-11813-2018-supplement
© Author(s) 2018. This work is distributed under
the Creative Commons Attribution 4.0 License.

Atmospheric Chemistry and Physics
Open Access
EGU

Supplement of

Implementing microscopic charcoal particles into a global aerosol–climate model

Anina Gilgen et al.

Correspondence to: Anina Gilgen (anina.gilgen@env.ethz.ch)

The copyright of individual parts of the supplement might differ from the CC BY 4.0 License.

S1 Charcoal properties

S1.1 Aspect ratio of charcoal

In the following, we summarise findings about the aspect ratio R of microscopic charcoal particles and how we derive from those estimates for the equivalent radius r_{eq}. The measurements by Clark and Hussey (1996) show a distinct maximum for aspect ratios $R = 1.5$-2, and the mean aspect ratio is 2.36 ± 1.53. While Clark and Hussey (1996) used 9 sites in temperate eastern North America for their analysis, Tinner and Hu (2003) studied charcoal particles from different biomes, namely Lago di Origlio (Switzerland; warm-temperate chestnut forest), Grizzly Lake (Alaska; spruce forest), and Wien Lake (Alaska; shrub birch tundra, poplar forest, and boreal forest). For the three sites, they report aspect ratios of $R = 1.9$, $R = 1.7$, and $R = 1.6$, respectively. Crawford and Belcher (2014) measured the aspect ratios of both microscopic and macroscopic charcoal particles. For microscopic charcoal (D_{M} up to 100 µm), they found aspect ratios of 1.8 and 2.4 for charcoal from wood and grass, respectively. It is worth mentioning that they used a cross-sectional area of 315 µm^2 as the lower threshold, which corresponds to a D_M of about $11.5 - 13.4$ µm for wood and $13.2 - 15.5$ µm for grass (assuming rectangual/elliptical cross-sections), i.e. a slightly larger D_{M} than the threshold of 10 µm used in this study.

All of these measurements of R lie in the same range. For our study, we chose $R = 2$ as an initial estimate. The third, non-visible dimension of the particle is expected to be smaller or equal to D_{m} for particles detected in pollen slides since the particles may tend to lie flat on the slides (Clark and Hussey 1996). For simplicity, we describe the shape of the charcoal particles with a rectangual cuboid (see Clark and Hussey 1996). Assuming that the non-visible axis equals the minor axis D_{m} (which is rather an upper estimate), the equivalent-volume radius r_{eq} is given by:

$$V_{\mathrm{cuboid}} = V_{\mathrm{sphere}} \tag{1}$$

$$D_{\mathrm{M}} \cdot \frac{D_{\mathrm{M}}}{R} \cdot \frac{D_{\mathrm{M}}}{R} = \frac{4}{3} \cdot \pi \cdot r_{\mathrm{eq}}^3 \tag{2}$$

$$\rightarrow r_{\mathrm{eq}} \approx 0.62 \cdot \frac{D_{\mathrm{M}}}{R^{\frac{2}{3}}}, \tag{3}$$

where V stands for volume. The typical lower threshold for microscopic charcoal particles is $D_{\mathrm{M}} = 10$ µm, which corresponds to an equivalent-volume radius of $r_{\mathrm{eq}} \approx 3.9$ µm. However, since the aspect ratio tends to increase with charcoal size (Crawford and Belcher 2014), R of the lower threshold ($D_{\mathrm{M}} = 10$ µm) might be smaller than the mean or median R for $D_{\mathrm{M}} > 10$ µm. In the model, we cannot account for a size-dependent R. For this study, it is important that the lower threshold of the counted and simulated charcoal particles match well since these small particles have higher number concentrations than larger particles (Clark and Hussey 1996; Tinner et al. 1998). As a lower estimate for our test simulations, we therefore use $R = 1.33$, which corresponds to the often applied, observation-based threshold of 75 µm^2 for microscopic charcoal cross-sections (e.g. Tinner et al. 2006) and which results in $r_{\mathrm{eq}} = 4.9$ µm. Based on the before mentioned observations from Clark and Hussey (1996) and Crawford and Belcher (2014), $R = 2.4$ is considered to be an upper bound, which corresponds to $r_{\mathrm{eq}} = 3.5$ µm.

S1.2 Radiative index of charcoal

Many studies (e.g. Habib and Vervisch 1988) report that higher H-C ratios result in a smaller imaginary part of RI, i.e. in a smaller absorption component. However, Bond and Bergstrom (2006) reviewed the radiative properties of different carbon-containing substances with focus on light-absorbing aerosol particles and found that the number of sp^2 bonds (more precisely: the

extent of sp^2-islands) matters most. More sp^2-islands result in higher absorption because sp^2-bonded carbon is arranged in planar layers, which allows the π-electrons to move freely. Although the light absorption is closely related to the imaginary part of RI, it is important to note that absorption also impacts the real part. It is therefore not possible to estimate the imaginary part independently of the real part.

In general, measured RIs of light-absorbing carbonaceous substances show a high variability caused by different burning conditions (Bond and Bergstrom 2006). In our opinion, charcoal particles should share some of the radiative properties of coal with similar H-C and O-C ratios (i.e. very low-ranked coal). If we slightly extend the "coal rank" line in Fig. 7 from Bond and Bergstrom (2006) to the H-C and O-C ratios of charcoal, we arrive at a refractive index of $\mathrm{RI} \approx 1.75 - 0.1k$ (for a wavelength of 550 nm). Unfortunately, this approach does not give us any information about the wavelength dependence of RI. However, the imaginary part of RI should not matter as much as the particle size: the charcoal particles are large compared with the dominant wavelengths of sunlight. If the absorption is relatively high, it is expected that no light penetrates to the interior of the particle, so that only the "skin" of the particle absorbs and all light encountering the particle skin is attenuated (Tami Bond, personal communication). The aerosol absorption in our model scales with the aerosol mass and does therefore not account for this. Hence we would overestimate the absorption by charcoal when using $\mathrm{RI} \approx 1.75 - 0.1k$. When we conducted 5-year test simulations with different RI for charcoal (once using RI from BC, once RI from dust), we did not detect clear differences in the atmospheric lifetime of charcoal between the model simulations. The RI of charcoal is therefore likely not important for its atmospheric transport. In the end, we decided to use the same RI as for dust ($\mathrm{RI} \approx 1.52 - 1.1 \times 10^{-3}k$); the lower absorption component of dust compared to charcoal should counteract that only part of the charcoal mass is expected to absorb radiation.

In our simulations, we found that the vertically integrated charcoal mass in the atmosphere is approximately one order of magnitude smaller than the mass of dust (using the chosen parameter set). Therefore, charcoal only contributes little to the total aerosol absorption optical thickness in our simulations. However, our simplified approach is very uncertain and does also not consider the non-sphericity of charcoal particles. If the absorption of charcoal were larger than with our simplified estimate, the contribution to the aerosol absorption optical depth might be somewhat higher, although we do not expect it to be large.

S2 Model implementation of charcoal

S2.1 In-cloud produced sulfate

Sulfate aerosols can be produced in cloud droplets when SO_2 reacts with O_3 or H_2O_2. When cloud droplets evaporate, aerosol particles remain, the size of which depends on the mass and chemistry of the foreign material in the cloud droplets (Mitra et al. 1992). The reaction with H_2O_2 is considered to be the dominant pathway (Seinfeld and Pandis 2006). Since the H_2O_2 concentration is often the limiting factor for the reaction with SO_2, most of sulfate is added to those particles activated early in the cloud, i.e. the best cloud condensation nuclei (Harris et al. 2014). Therefore, we distribute the sulfate mass produced in-cloud among the larger soluble aerosol modes (accumulation, coarse, and giant) in case these modes exist. If none of the three modes exist, a new soluble coarse mode is created.

S2.2 Gravitational settling

To ensure numerical stability in aerosol gravitational settling, aerosol particles can only cross one model layer within one timestep. However, only size distributions with large geometric mean radii close to the surface, where the model layers are thin, are affected. We expect that this velocity restriction might delay gravitational settling for large geometric mean radii by up to

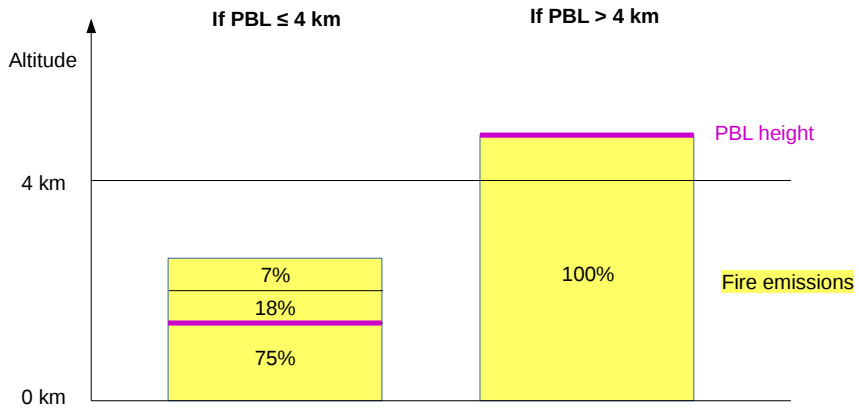

Figure S1: Illustration of fire emission heights in ECHAM6-HAM2.

a few time steps near the surface. However, this should not considerably change the spatial gravitational settling pattern since particles are not transported far horizontally within this time (as the horizontal scale of the grid is much larger than the vertical scale and horizontal wind velocities are rather low near the surface). Furthermore, only a very small number of charcoal size distributions have a sufficiently large geometric mean radius to be impacted.

S2.3 Calculation of number fluxes above threshold radius

To compare the simulated charcoal fluxes with observations, it is essential that only simulated fluxes of particles with $D_{\mathrm{M}} > 10\,\mu\mathrm{m}$ are considered. We calculated the total number of charcoal particles above this threshold directly before and after the calculation of the removal processes (gravitational settling, dry deposition, wet deposition). From the difference, we calculate the fluxes to the surface as illustrated in Supplementary Fig. S2.

Since the observations only consider pure charcoal particles, we should only take the charcoal component of the soluble giant mode into account when comparing to observations. Therefore, knowledge about the size distribution of the charcoal component is important. Our model assumes an ideal internal aerosol mixture, i.e. the total number of particles for the soluble giant mode is also representative for the number of charcoal particles in the soluble giant mode. The charcoal mass on the other hand is only a fraction of the total soluble giant mode mass (e.g. sulfate in addition). Hence, the number size distribution of the charcoal particles in the soluble giant mode is shifted to smaller radii compared to the total soluble giant mode but also follows a log-normal distribution with the same σ as the total soluble giant mode (see Supplementary Fig. S3).

Due to a small inconsistency in the code, small negative surface fluxes can occur: the radius used to calculate the removal processes is only updated once per timestep, while the number and mass tracer tendencies are updated inbetween. Since we use the tracer tendencies to calculate the radius before and after the removal process, our diagnostics do not use exactly the same radius as the calculations for the removal processes do. However, the error is negligible compared to the mean surface fluxes.

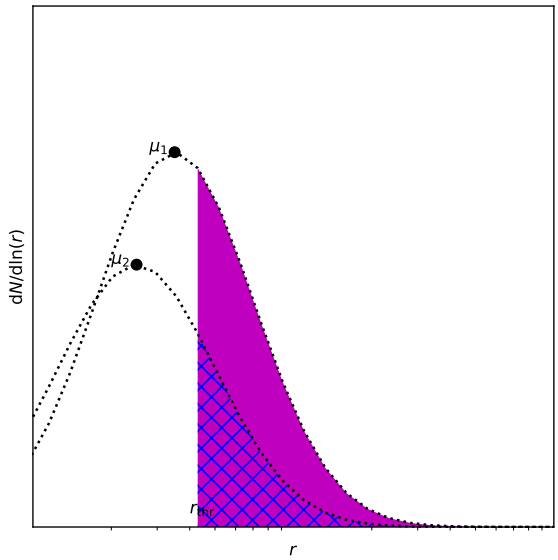

Figure S2: Illustration of how the deposition of charcoal particles above a certain threshold radius (r_{thr}) was calculated. Before the removal process (e.g. gravitational settling), the number geometric mean radius of a gridbox is μ_1. The number concentration of particles above the threshold radius is proportional to the area below the curve, i.e. the magenta area. After the removal process, both the number geometric mean radius and the total number concentration change (shift to μ_2). Now the hatched area represents the particle number concentration above the threshold radius. From the difference between the magenta and the hatched area we can calculate how many charcoal particles are removed. Number fluxes are then calculated by dividing by the time step and the area of the gridbox.

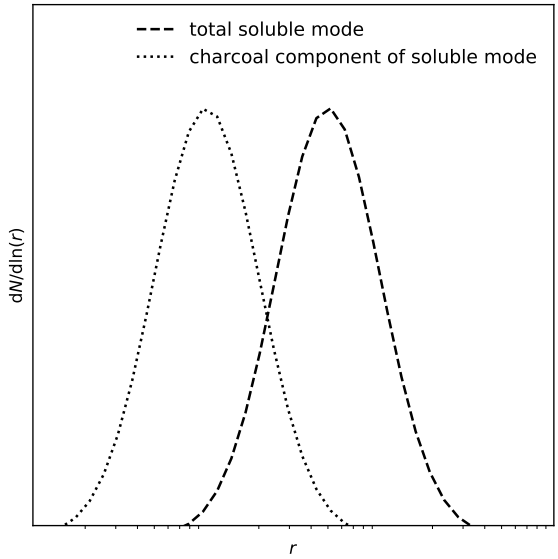

Figure S3: Schematic number size distribution of the total soluble giant mode and its charcoal component.

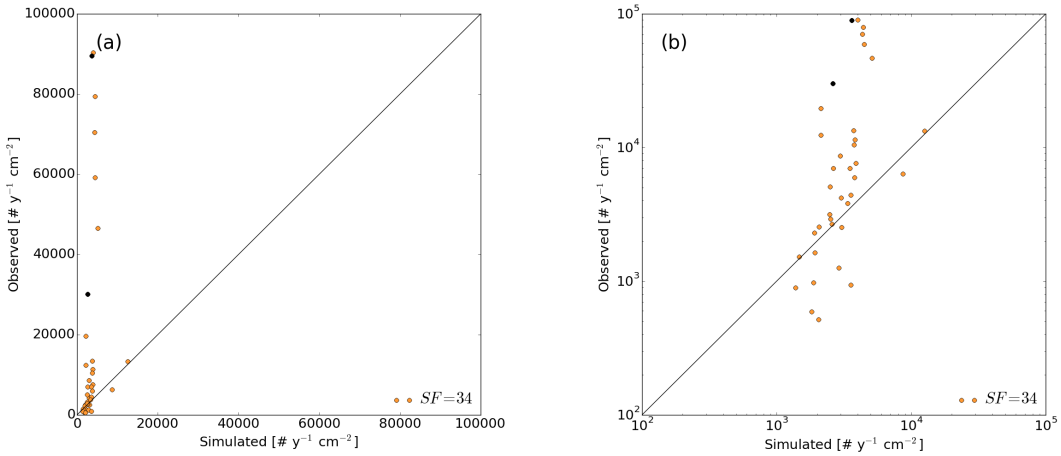

Figure S4: An example of the simulated versus observed number fluxes of charcoal particles above the threshold radius (in $\mathrm{cm^{-2}\,y^{-1}}$) (a) on a linear scale and (b) on a logarithmic scale. The two black points show the sites likely influenced by surface runoff. The following parameters were used in this simulation: an emission number geometric mean radius of $r_{\mathrm{eq}} = 2.5\,\mu\mathrm{m}$, a threshold radius of $r_{\mathrm{eq}} = 3.9\,\mu\mathrm{m}$, and a charcoal density of $0.5\,\mathrm{g\,cm^{-3}}$. The scaling factor is $SF = 34$.

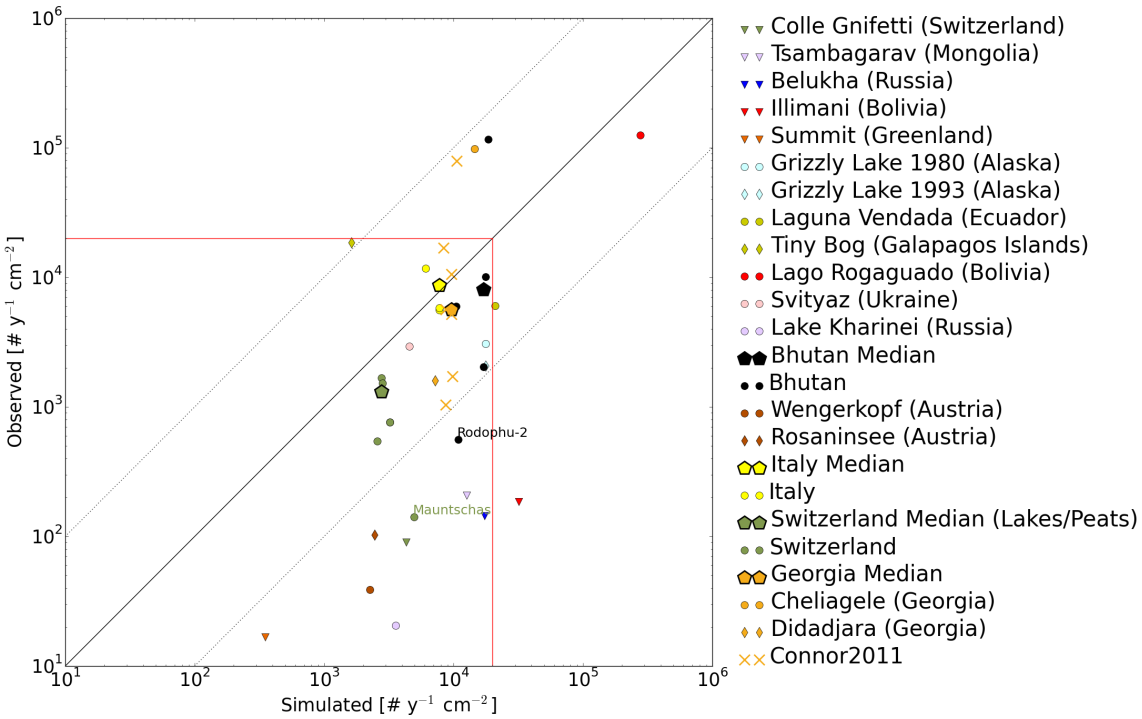

Figure S5: The same as Fig. 5 in the paper but for the free instead of the nudged model simulation.

Table S1: An overview of the observation sites from the calibration dataset (Adolf et al. 2018). The data is sorted alphabetically by country.

Site	Country	Longitude [°]	Latitude [°]	Altitude [m ASL]	Lake size [ha]
Černé jezero	Czech Republic	13.18	49.18	1007	18.4
Hromnické jezírko	Czech Republic	13.44	49.85	332	2
Étang d'Entressen	France	4.92	43.6	34	103.5
Lac du Crès	France	3.93	43.65	39	6
Holzmaar	Germany	6.88	50.12	422	20
Limni Kournas	Greece	24.27	35.33	18	42.0
Biviere di Gela	Italy	14.35	37.02	0	150
Gorgo Basso	Italy	12.66	37.61	27	3
Lago dell'Accesa	Italy	10.9	42.99	111	16
Lago dello Scanzano	Italy	13.37	37.92	547	97
Lago di Baratz	Italy	8.23	40.68	24	60
Lago di Pergusa	Italy	14.31	37.52	677	50
Lago di Varese	Italy	8.72	45.83	240	1480
Lago Piccolo d'Avigliana	Italy	7.4	45.05	288	61.1
Specchio di Venere	Italy	11.99	36.82	8	19.4
Jezioro Gołyń	Poland	15.78	52.44	26	9.5
Jezioro Gościąż	Poland	19.34	52.58	76	42
Suchar II	Poland	23.02	54.09	140	2.5
Lagoa Escura	Portugal	-7.64	40.36	1679	2
Lago Enol	Spain	-4.99	43.27	1077	12.2
Laguna Conceja	Spain	-2.81	39.93	857	29.4
Laguna de Taravilla	Spain	-1.97	40.65	1113	2.1
Laguna Grande de Estaña	Spain	-0.53	42.02	669	18.8
Laguna Zóñar	Spain	-4.69	37.48	301	37
Hagsjön	Sweden	13.69	57.26	170	22.2
Sarsjön	Sweden	19.6	64.04	274	7.78
Sisstjärnen	Sweden	14.92	60.65	216	9.6
Stora Utterträsk	Sweden	20.41	66.12	277	28.1
Vuolep Njakajaure	Sweden	18.78	68.34	408	30
Gerzensee	Switzerland	7.55	46.83	603	25.2
Iffigsee	Switzerland	7.41	46.39	2065	10
Lac du Mont d'Orge	Switzerland	7.34	46.23	595	3
Lago d'Origlio	Switzerland	8.94	46.05	423	8
Lej da San Murezzan	Switzerland	9.85	46.49	1773	78
Mauensee	Switzerland	8.07	47.17	500	51
Soppensee	Switzerland	8.08	47.09	593	24
Blue Lake	Ukraine	33.2	48.45	87	24.4

Table S2: A summary of the different observation sites used for validation. Note that the youngest date of the record is given as *calibrated* years for the ^{14}C method. Most data was taken from the Alpine Pollen Database of University of Bern (ALPADABA). The sorting follows the legend of Fig. 3.

Site	Country	Lon [°]	Lat [°]	Altitude [m ASL]	Time period	Record type	Dating method	Dated material	Youngest date	Lake size [ha]	Publication
Colle Gnifetti	Switzerland	7.88	45.93	4450	2002-2015	Ice core	Annual layer counting	-	-	-	This study
Tsambagarav	Mongolia	90.85	48.66	4130	1988-2009	Ice core	Annual layer counting	-	-	-	This study
Belukha	Russia	86.59	49.81	4062	Mean of two samples (1987, 1996/97)	Ice core	Annual layer counting	-	-	-	Eichler et al. (2011)
Illimani	Bolivia	-67.78	-16.65	6300	2008-2015	Ice core	Annual layer counting	-	-	-	This study
Summit	Greenland	-38.46	72.58	3200	1989 core	Ice core	Surface probe	-	-	-	This study
Grizzly Lake	Alaska	-144.19	62.71	720	1980, summer 1993	Lake	^{210}Pb	Bulk	AD1992-1994	11	Tinner et al. (2006)
Laguna Vendada	Ecuador	-79.39	-3.61	3640	2009	Peat	^{14}C	Terrestrial macrofossil	AD943 ± 35	2	This study
Tiny Bog	Galapagos Islands (Ecuador)	-90.33	0.64	819	2005	Peat	^{14}C	Sphagnum	More recent than AD1950	0.01	This study

Lago Rogaguado	Bolivia	-65.93	-13.02	125	2004	Lake	^{14}C	Terrestrial macrofossil	AD1543 ±84	31500	Brugger et al. (2016)
Svityaz	Ukraine	23.84	51.50	157	2004	Lake	^{14}C	Terrestrial macrofossil	AD1139 ± 110	2519	This study
Lake Kharinei	Russia	62.75	67.37	110	Summer 1993	Lake	^{210}Pb	Bulk	AD2003	5	Salonen et al. (2011)
Tergang	Bhutan	91.07	27.83	2260	Summer 1992	Peat	^{14}C	Bulk	AD1097	Very small	This study
Shamling	Bhutan	91.12	27.77	2350	1990	Lake/peat	^{14}C	Terrestrial macrofossil	AD1807	-	This study
Rodophu-2	Bhutan	89.78	28.05	4530	2000	Lake/peat	^{14}C	Bulk	AD1189	-	This study
Laya	Bhutan	89.68	28.07	3830	2000	Lake/peat	^{14}C	Terrestrial macrofossil	AD1723	-	This study
Singhe Dzong	Bhutan	91.32	27.97	3800	2000	Peat	^{14}C	Terrestrial macrofossil	AD1248	Very small	P. Kunes
Wengerkopf	Austria	13.87	47.17	1780	Summer 2001	Peat	^{210}Pb	Bulk	AD1996	0.3	Knaap et al. (2012)
Rosaninsee	Austria	13.78	46.95	2070	Summer 2001	Peat	^{210}Pb	Bulk	AD1993	0.3	Knaap et al. (2012)
Gorgo Basso	Italy	12.65	37.62	6	2001	Lake	^{14}C	Terrestrial macrofossil	AD1772	3	Tinner et al. (2009)
Gorgo Lungo di Ficuzza	Italy	13.41	37.90	877	2003	Lake	^{14}C	Terrestrial macrofossil	AD755	0.2	Tinner et al. (2016)
Gorgo Tondo di Ficuzza	Italy	13.41	37.90	783	2006	Lake	^{14}C	Terrestrial macrofossil	AD1280	0.6	Tinner et al. (2016)
Etang de la Gruère	Switzerland	7.05	47.24	1005	1993	Peat	^{14}C	Terrestrial macrofossil	AD1809	22.5	Public data (counted by van Leeuwen)
Mauntschas	Switzerland	9.85	46.49	1819	2003	Peat	^{14}C	Sphagnum	AD1988	10	Knaap et al. (2012)

Les Amburnex	Switzerland	6.23	46.54	1375	2000	Peat	^{14}C	Terrestrial macrofossil	AD1770	0.2	Sjögren and Lamentowicz (2008)
Sèche de Gimel	Switzerland	6.23	46.54	1300	2003	Peat	^{14}C	Terrestrial macrofossil	AD1995	12	Sjögren (2005)
Le Moé	Switzerland	6.22	46.54	1310	2002	Peat	^{14}C	Sphagnum and Polytrichum stems	AD1991	12	Sjögren (2006)
Hallwilersee	Switzerland	8.21	47.28	400	Summer 1998	Lake	Annual layer counting	-	-	1030	This study
Lac de Bretaye	Switzerland	7.07	46.33	1780	2012	Lake	^{14}C	Terrestrial macrofossil	BC82	4	Thöle et al. (2016)
Cheliagele	Georgia	43.11	42.62	1100	Summer 1992	Lake/peat	^{14}C	-	AD1949	-	This study
Didadjara	Georgia	42.5	41.67	1850	2000	Lake/peat	^{14}C	-	AD859	-	Connor et al. (2017, submitted)
Sakhare	Georgia	45.32	41.58	800	2000	Lake	^{14}C	Bulk	AD500 ± 80	12	Connor (2011)
Kumisi	Georgia	44.83	41.58	469	2000	Lake	^{14}C	Bulk	AD800 ± 40	120	Connor (2011)
Tsavkisi	Georgia	44.75	41.68	1110	2000	Peat	^{14}C	Isolated pollen	AD530 ± 60	4	Connor (2011)
Imera	Georgia	44.2	41.65	1610	2000	Lake	^{14}C	Bulk	AD940 ± 40	12	Connor (2011)
Bareti	Georgia	44.17	41.65	1630	1986	Lake	^{14}C	Bulk	AD1050 ± 40	62	Connor (2011)

Jvari	Georgia	44.73	41.83	570	2000	Lake	Correlation with neigh-bouring sites	-	-	9.6	Connor (2011)
Aligol	Georgia	44.02	41.63	1534	2000	Lake	^{14}C	Bulk	AD1760 $\pm$ 40	9.6	Connor (2011)

References

Adolf, C., S. Wunderle, D. Colombaroli, H. Weber, E. Gobet, O. Heiri, J. F. N. van Leeuwen, C. Bigler, S. E. Connor, M. Gałka, T. La Mantia, S. Makhortykh, H. Svitavská-Svobodová, B. Vannière, and W. Tinner (2018). "The sedimentary and remote-sensing reflection of biomass burning in Europe". In: *Global Ecol. Biogeogr.* 27.2, pp. 199–212. DOI: 10.1111/geb.12682.

Bond, T. C. and R. W. Bergstrom (2006). "Light Absorption by Carbonaceous Particles: An Investigative Review". In: *Aerosol Sci. Tech.* 40.1, pp. 27–67. DOI: 10.1080/02786820500421521.

Brugger, S. O., E. Gobet, J. F. van Leeuwen, M.-P. Ledru, D. Colombaroli, W. van der Knaap, U. Lombardo, K. Escobar-Torrez, W. Finsinger, L. Rodrigues, A. Giesche, M. Zarate, H. Veit, and W. Tinner (2016). "Long-term man–environment interactions in the Bolivian Amazon: 8000 years of vegetation dynamics". In: *Quaternary Sci. Rev.* 132, pp. 114–128. ISSN: 0277-3791. DOI: 10.1016/j.quascirev.2015.11.001.

Clark, J. S. and T. C. Hussey (1996). "Estimating the mass flux of charcoal from sedimentary records". In: *The Holocene* 6.2, pp. 129–144.

Connor, S., D. Colombaroli, F. Confortini, E. Gobet, B. Ilyashuk, I. E., J. van Leeuwen, M. Lamentowicz, W. van der Knaap, E. Malysheva, A. Marchetto, N. Margalitadze, Y. Mazei, E. Mitchell, R. Payne, and B. Ammann (2017). "Long-term population dynamics – theory and reality in a peatland ecosystem". In: *J. Ecol.*

Connor, S. E. (2011). *A Promethean Legacy: Late Quaternary Vegetation History of Southern Georgia, the Caucasus*. Peeters, Louvain.

Crawford, A. and C. Belcher (2014). "Charcoal Morphometry for Paleoecological Analysis: The Effects of Fuel Type and Transportation on Morphological Parameters". In: *Appl. Plant. Sci.* 2.8, pp. 1–10. DOI: 10.3732/apps.1400004.

Eichler, A., W. Tinner, S. Brütsch, S. Olivier, T. Papina, and M. Schwikowski (2011). "An ice-core based history of Siberian forest fires since AD 1250". In: *Quaternary Sci. Rev.* 30.9–10, pp. 1027–1034. ISSN: 0277-3791. DOI: 10.1016/j.quascirev.2011.02.007.

Habib, Z. and P. Vervisch (1988). "On the refractive index of soot at flame temperature". In: *Combust. Sci. Tech.* 59, pp. 261–274.

Harris, E., B. Sinha, D. van Pinxteren, J. Schneider, L. Poulain, J. Collett, B. D'Anna, B. Fahlbusch, S. Foley, K. Fomba, C. George, T. Gnauk, S. Henning, T. Lee, S. Mertes, A. Roth, F. Stratmann, S. Borrmann, P. Hoppe, and H. Herrmann (2014). "In-cloud sulfate addition to single particles resolved with sulfur isotope analysis during HCCT-2010". In: *Atmos. Chem. Phys.* 14, pp. 4219–4235.

Knaap, W. O. van der, J. F. N. van Leeuwen, T. Goslar, R. Krisai, and W. Tinner (2012). "Human impact on vegetation at the Alpine tree-line ecotone during the last millennium: lessons from high temporal and palynological resolution". In: *Veg. Hist. Archaeobot.* 21.1, pp. 37–60. ISSN: 09396314, 16176278.

Mitra, S., J. Brinkmann, and H. Pruppacher (1992). "A wind tunnel study on the drop-to-particle conversion". In: *J. Aerosol Sci.* 23.3, pp. 245–256. ISSN: 0021-8502. DOI: 10.1016/0021-8502(92)90326-Q.

Salonen, J. S., H. Seppä, M. Väliranta, V. J. Jones, A. Self, M. Heikkilä, S. Kultti, and H. Yang (2011). "The Holocene thermal maximum and late-Holocene cooling in the tundra of NE European Russia". In: *Quaternary Res.* 75.3, pp. 501–511. ISSN: 0033-5894. DOI: 10.1016/j.yqres.2011.01.007.

Seinfeld, J. and S. Pandis (2006). *Atmospheric Chemistry and Physics: From Air pollution to Climate Change*. Hoboken, New Jersey: John Wiley & Sons, Inc. ISBN: 978-0-471-72018-8.

Sjögren, P. (2005). "Palaeoecological investigatons of pasture woodland in Combe des Amburnex, Swiss Jura Mountains". PhD thesis. Institut für Pflanzenwissenschaften, Bern.

Sjögren, P. (2006). "The development of pasture woodland in the southwest Swiss Jura Mountains over 2000 years, based on three adjacent peat profiles". In: *The Holocene* 16.2, pp. 210–223. DOI: 10.1191/0959683606hl921rp.

Sjögren, P. and M. Lamentowicz (2008). "Human and climatic impact on mires: a case study of Les Amburnex mire, Swiss Jura Mountains". In: *Veg. Hist. Archaeobot.* 17.2, pp. 185–197. ISSN: 1617-6278. DOI: 10.1007/s00334-007-0095-9.

Thöle, L., C. Schwörer, D. Colombaroli, E. Gobet, P. Kaltenrieder, J. van Leeuwen, and W. Tinner (2016). "Reconstruction of Holocene vegetation dynamics at Lac de Bretaye, a high-mountain lake in the Swiss Alps". In: *The Holocene* 26.3, pp. 380–396. DOI: 10.1177/0959683615609746.

Tinner, W., M. Conedera, B. Ammann, H. W. Gaggeler, S. Gedye, R. Jones, and B. Sagesser (1998). "Pollen and charcoal in lake sediments compared with historically documented forest fires in southern Switzerland since AD 1920". In: *The Holocene* 8.1, pp. 31–42.

Tinner, W. and F. S. Hu (2003). "Size parameters, size-class distribution and area-number relationship of microscopic charcoal: relevance for fire reconstruction". In: *The Holocene* 13.4, pp. 499–505. DOI: 10.1191/0959683603hl615rp.

Tinner, W., F. S. Hu, R. Beer, P. Kaltenrieder, B. Scheurer, and U. Krähenbühl (2006). "Post-glacial vegetational and fire history: pollen, plant macrofossil and charcoal records from two Alaskan lakes". In: *Veg. Hist. Archaeobot.* 15.4, pp. 279–293. ISSN: 09396314, 16176278.

Tinner, W., J. F. van Leeuwen, D. Colombaroli, E. Vescovi, W. van der Knaap, P. D. Henne, S. Pasta, S. D'Angelo, and T. L. Mantia (2009). "Holocene environmental and climatic changes at Gorgo Basso, a coastal lake in southern Sicily, Italy". In: *Quaternary Sci. Rev.* 28.15–16, pp. 1498–1510. ISSN: 0277-3791. DOI: 10.1016/j.quascirev.2009.02.001.

Tinner, W., E. Vescovi, J. F. N. van Leeuwen, D. Colombaroli, P. D. Henne, P. Kaltenrieder, C. Morales-Molino, G. Beffa, B. Gnaegi, W. O. van der Knaap, T. La Mantia, and S. Pasta (Sept. 2016). "Holocene vegetation and fire history of the mountains of Northern Sicily (Italy)". In: *Veg. Hist. Archaeobot.* 25.5, pp. 499–519. DOI: 10.1007/s00334-016-0569-8.